



Optimizing Interface Conductivity in Electronics



The latest eBook from
Advanced Optical Metrology.
Download for free.

Surface roughness is a key parameter for judging the performance of a given material's surface quality for its electronic application. A powerful tool to measure surface roughness is 3D laser scanning confocal microscopy (LSM), which will allow you to assess roughness and compare production and finishing methods, and improve these methods based on mathematical models.

Focus on creating high-conductivity electronic devices with minimal power loss using laser scanning microscopy is an effective tool to discern a variety of roughness parameters.

EVIDENT
OLYMPUS

WILEY

Interplay Between Doping, Morphology, and Lattice Thermal Conductivity in PEDOT:PSS

Paolo Sebastiano Floris,* Claudio Melis, and Riccardo Rurali*

Organic materials for thermoelectric (TE) applications have attracted a fair amount of attention in recent years due to remarkable advances achieved in terms of their figure of merit, ZT: a value of 0.42 has been reported by for poly(3,4-ethylenedioxythiophene) polystyrene sulfonate (PEDOT:PSS) films treated with dimethyl sulfoxide, while 0.25 has been obtained for PEDOT:Tosylate. In this study various PEDOT morphologies are investigated, considering both neutral and doped (bipolaronic) samples, by means of classical molecular dynamics, by taking advantage of a recently developed all-atom force field. In the case of bare PEDOT, it is found that changing the distribution of chain lengths affects the thermal conductivity of neutral and doped samples in a different way: longer chain lengths result in higher conductivities in the neutral scenario, whereas an intermediate chain length gives the highest value in the bipolaronic case. The role of PSS in the bipolaronic state, as compared to the simpler case where the counterion is Cl^- , is discussed.

biosensors,^[6] flexible electronics^[7,8] and thermoelectric generators (TEGs).^[9–13] Regarding the latter, although pristine PEDOT:PSS shows low electrical conductivity (σ , around $0.1\text{--}1\text{ S cm}^{-1}$), this value can be increased up to three orders of magnitude through careful doping and post-processing with organic polar solvents with high boiling point, such as dimethyl sulfoxide (DMSO).^[14] Furthermore, PEDOT:PSS has an intrinsically low thermal conductivity, κ , which is reported to be between 0.17 and $0.37\text{ W m}^{-1}\text{ K}^{-1}$.^[15] Promising values of the TE figure of merit (ZT) have been reported in literature for PEDOT composites, such as 0.25 in PEDOT:Tosylate,^[16] 0.42 in PEDOT:PSS^[17] and 0.75 in heterostructures with ionic liquids on top of the polymer surface.^[18]

Computational modeling has been widely used to investigate PEDOT:PSS,


with methods that range from Density Functional Theory (DFT)^[19–23] to Molecular Dynamics (MD)^[20,22–26] and Coarse Grained MD.^[27,28] These techniques have the potential to uncover theoretical and practical insights that would be otherwise complicated (if not currently impossible) to access experimentally. For instance, it has been possible to shed light on the mechanism underlying the enhancement of σ upon treatment with DMSO, which dissolves the PSS shells and facilitates the aggregation of PEDOT chains.^[20] It has also been demonstrated that the morphology of PEDOT:PSS solutions is strongly dependent on pH (and therefore on the protonation level of PSS molecules) in that both low pH and $\text{pH} \approx 5$ tend to favor granular morphologies (a PEDOT core surrounded by a PSS insulating shell), while $\text{pH} \approx 2.5$ results in homogeneous morphologies of PEDOT oligomers surrounded by a PSS matrix.^[27] Thermal properties of pristine PEDOT have also been studied: Crnjar *et al.*^[24] found that single 1D PEDOT chains exhibit anomalous superdiffusive thermal transport, but this feature disappears when considering perfect 3D crystals. In another work, Genovese *et al.*^[25] investigated the connection between morphological features and thermal conductivity, finding that crystalline and amorphous regions have high and low thermal conductivity, respectively, which is directly proportional to the length of the oligomers contained in the sample, irrespective of morphology. Shi *et al.* argue in their work^[21] that, although the TE power factor ($S^2\sigma$, where S is the Seebeck coefficient), is maximized along the backbone direction, lattice thermal conductivity is lower in the chain stacking direction by 2 orders of magnitude, which leads to a better TE performance.

1. Introduction

Since the groundbreaking discovery of conducting polymers with the synthesis of iodine doped polyacetylene in 1977,^[1] many other materials with similar and improved properties have been designed. Poly(3,4-ethylenedioxythiophene) (PEDOT), in conjunction with polystyrene sulfonate (PSS) as its counterion, has emerged as one of the most interesting and it has been employed in a fairly wide range of applications including, but not limited to, Organic Field Effect Transistors (OFETs),^[2] Organic Light Emitting Diodes (OLEDs),^[3] photovoltaic cells,^[4,5]

P. S. Floris, R. Rurali
Institut de Ciència de Materials de Barcelona
ICMAB-CSIC
Campus UAB, 08193 Bellaterra, Spain
E-mail: pfloris@icmab.es; rrurali@icmab.es

C. Melis
Dipartimento di Fisica
Università di Cagliari
Cittadella Universitaria, Monserrato, I-09042 Cagliari, Italy

 The ORCID identification number(s) for the author(s) of this article can be found under <https://doi.org/10.1002/adfm.202215125>.

© 2023 The Authors. Advanced Functional Materials published by Wiley-VCH GmbH. This is an open access article under the terms of the Creative Commons Attribution-NonCommercial-NoDeriv License, which permits use and distribution in any medium, provided the original work is properly cited, the use is non-commercial and no modifications or adaptations are made.

DOI: 10.1002/adfm.202215125

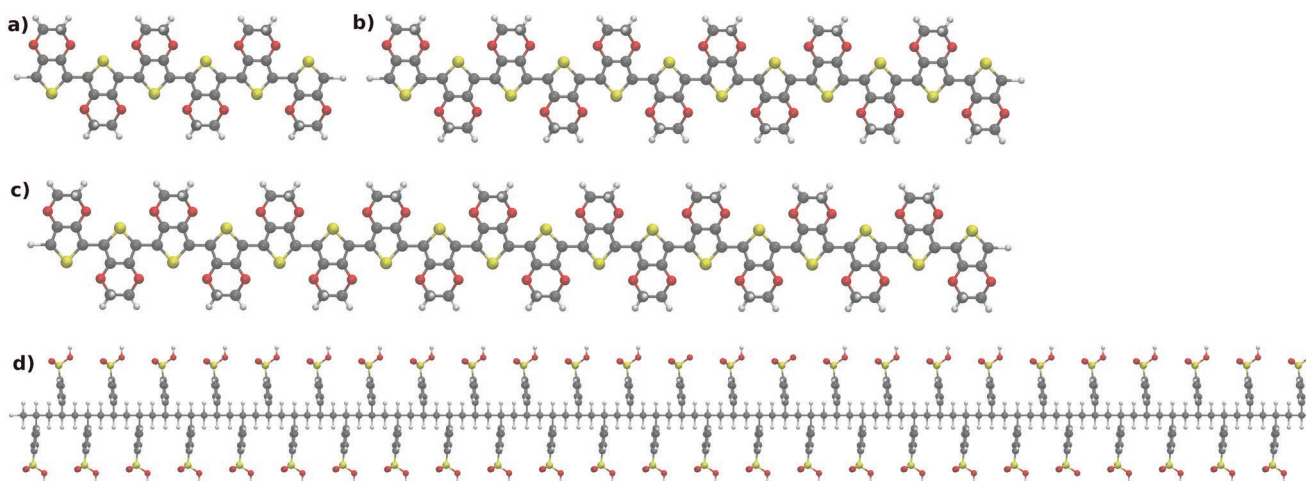


Figure 1. a–c) Graphical representations of three PEDOT molecules with varying chain lengths (6, 12, and 18 monomers). d) A PSS molecule made of 50 monomers. The Visual Molecular Dynamics (VMD) software,^[29] in conjunction with Tachyon,^[30] is used to generate images from MD simulation files throughout the present work.

Additionally, their findings enforce the need to investigate high mobility polymers since high carrier concentrations upon doping are detrimental to the Seebeck coefficient.

In this work, we study the effect of chain length composition of PEDOT samples on its lattice thermal conductivity. We consider samples with different distribution of chain lengths (all the molecules employed are represented in **Figure 1**) and we assess the effect of the charges introduced in the PEDOT backbone upon doping, addressing separately the case study of a simple counterion, such as Cl^- , and of its polyanionic counterion, PSS. To this end, we carry out fully atomistic approach-to-equilibrium molecular dynamics (AEMD), relying on a newly developed force field that has been specifically parameterized to describe undoped and highly doped PEDOT, bypassing some of the shortcomings of more conventional force fields used in the past. These results are accompanied by a detailed structural analysis, including simulations of X-ray diffraction spectra, in order to look for possible correlations with the computed thermal conductivities and to validate the morphologies obtained, comparing them with available experimental results.

2. Computational Methods

2.1. Force Field

We use a new atomistic force field for undoped and highly doped PEDOT developed by Michaels *et al.*^[19,26] The force field is parameterized using DFT calculations of molecular geometries, vibrational energies, and torsional profiles.^[19] This model intends to overcome some of the limitations of the Generalized AMBER Force Field (GAFF),^[31] a family of force fields that was developed for the simulation of a wide range of biomolecules, but that has not been thoroughly validated for PEDOT. In particular, the highly optimized force field here employed is capable to account for the differences in the ground-state geometry and torsional barriers of neutral and doped PEDOT, while GAFF predictions are rather similar in the two cases. In

this context, it is of great importance, as we will discuss below, the ability of this force field to capture the aromatic-to-quinoid transition that PEDOT undergoes upon doping. The fact that vibrational energies are reproduced with great accuracy is of particular relevance for the goal of the present study, that is, the calculation of the lattice thermal conductivity. To maintain compatibility with GAFF, in the model of Michaels *et al.* the potential energy takes the following form:

$$U = \sum_{\text{bonds}} k_b (r - r_0)^2 + \sum_{\text{angles}} k_\theta (\theta - \theta_0)^2 + \sum_{\text{dihedrals}} \frac{k_d}{2} \sum_{i=1}^n (1 + \cos(n\Phi - \Phi_0)) + \sum_{i < j} \left[\frac{q_i q_j}{4\pi\epsilon_0 r_{ij}} + 4\epsilon_{ij} \left(\left(\frac{\sigma_{ij}}{r_{ij}} \right)^{12} - \left(\frac{\sigma_{ij}}{r_{ij}} \right)^6 \right) \right] \quad (1)$$

where k_b (r_0), k_θ (θ_0), and k_d (Φ_0) are the force constants (equilibrium values) for bonds, angles, and dihedrals, respectively; n indicate the dihedral periodicity, q_i is the atomic partial charge and ϵ_0 is the dielectric constant of vacuum. ϵ_{ij} and σ_{ij} are the parameters of the Lennard–Jones (LJ) interaction. The Lorentz–Berthelot combining rule was used in this work for mixed interactions (i.e., $\sigma_{ij} = \frac{\sigma_{ii} + \sigma_{jj}}{2}$ and $\epsilon_{ij} = \sqrt{\epsilon_{ii}\epsilon_{jj}}$). All the LJ parameters are kept unaltered with respect to GAFF. The charges are calculated using the Restrained Electrostatic Potential (RESP) method.^[26] The cutoff for van der Waals interactions is set to 1 nm and a Particle–Particle Mesh (PPPM) solver is used for long-range electrostatic interactions throughout all simulations in this work.

2.2. Thermal Conductivity

We use approach-to-equilibrium molecular dynamics (AEMD), a method based on the lumped capacitance approximation, under which the lattice thermal conductivity, κ_l , can be extrapolated from the time constant of the exponential decay

of the temperature difference between two bodies at initial temperatures T_1 and T_2 .^[32,33] The simulation times are normally shorter than in nonequilibrium MD (NEMD) and no extensive configurational averaging is needed, as often prescribed in equilibrium MD (EMD). Besides its computational efficiency, this method has the conceptual advantage that it does not require the calculation of the heat flux. As a drawback, each simulation gives only access to the thermal conductivity along a specific transport direction, while within EMD the full thermal conductivity tensor is obtained at once.

In order to perform AEMD calculations, we define two regions in each sample, dividing it in half. Then, we bring the first half to $T_1 = 400$ K (10^5 steps of velocity rescaling with timestep $t_s = 0.5$ fs) and the second one to $T_2 = 200$ K (keeping the same parameters); once a step-like temperature profile is established, we let the system reach thermal equilibrium in the NVE ensemble. The number of steps needed to reach equilibrium varies according to the size and the thermal diffusivity; $1\text{--}2 \times 10^6$ timesteps are sufficient to reach $\Delta T(t) = \langle T_1 \rangle - \langle T_2 \rangle \sim 0$ in our systems, where $\Delta T(t)$ is the time dependent temperature difference and the brackets denote an ensemble average. In this case, the thermal equilibrium corresponds to the temperature $T_{eq} = 300$ K (given that the system is spatially uniform in the direction of heat transfer that we are considering, which is the case for all the systems discussed in this work) and thus the thermal conductivity that we calculate is $\kappa(T_{eq})$. If we consider the i -axis as the direction of heat transfer, the temperature difference between the two regions can be expressed as

$$\Delta T(t) = \langle T_1 \rangle - \langle T_2 \rangle = \sum_{n=1}^{\infty} C_n e^{-\alpha_n^2 \kappa_i t} \quad (2)$$

where $\langle T \rangle$ represents the average temperature of a region, $\alpha_n = \frac{2\pi n}{L_i}$, L_i is the length of the sample in the transport direction, κ_i is thermal diffusivity and

$$C_n = 8(T_1 - T_2) \frac{[\cos(\alpha_n L_i / 2) - 1]^2}{\alpha_n^2 L_i^2} \quad (3)$$

(in Supporting Information, we plot the time evolution of ΔT in a few representative cases). The lattice thermal conductivity is then obtained from

$$\kappa_i = \frac{\overline{\kappa_i} C_v}{V} \quad (4)$$

where C_v is the heat capacity, calculated according to the Dulong–Petit law

$$C_v = 3Nk_B \quad (5)$$

where N is the number of atoms present in the system. We repeated this procedure for all the samples, in each of the three Cartesian directions ($i = x, y, z$), and set the limit for the summation in Equation 2 to $n = 20$, which has been proven to be more than sufficient to obtain converged thermal conductivities.^[33] Due to the relatively low Debye temperature of PEDOT (315 K, see Ref. [34]), we did not consider any

Table 1. Summary of chain size distributions for pristine PEDOT.

| Sample name | PEDOT oligomers | | | L_{avg} [monomer units] | Total number of monomers |
|---------------------|-----------------|------|------|------------------------------|-----------------------------|
| | 6 | 12 | 18 | | |
| PEDOT ₆ | 3000 | 0 | 0 | 6 | 18000 |
| PEDOT ₁₂ | 0 | 1500 | 0 | 12 | 18000 |
| PEDOT ₁₈ | 0 | 0 | 1000 | 18 | 18000 |
| TRI ₆ | 1500 | 375 | 250 | 8.47 | 18000 |
| TRI ₁₂ | 750 | 750 | 250 | 10.29 | 18000 |
| TRI ₁₈ | 750 | 375 | 500 | 11.08 | 18000 |
| UNI | 1000 | 500 | 333 | 9.82 | 17994 |

quantum corrections taking into account the deviations from the Maxwell–Boltzmann distribution.

2.3. Sample Generation Procedure

All PEDOT samples were generated by randomly inserting the molecules in a cubic simulation box, using the LAMMPS software suite.^[35] The generation procedure consisted in defining the dimensions of the box in such a way that the initial density (ρ) would be somewhere around $0.6\text{--}0.8$ g cm⁻³, then letting the system evolve in the NPT ensemble at 300 K and 1 atm with a timestep of 0.5 fs, until it reached a stable configuration. A total time of 10 ns was enough to achieve convergence of both the density and the end-to-end chain length in all the systems investigated (see Supporting Information). PEDOT oligomers of 3 different sizes have been used in the calculations, consisting of 6, 12, and 18 repeating units. In the case of pristine PEDOT, seven samples with different chain length distributions (and therefore different average chain length, which we will denote as L_{avg}) have been created for both the neutral and doped scenario, as summarized in Table 1.

All such samples have a total of 18000 repeating units (except for sample 7, which has 17994). Samples 1–3 –from now on referred to as PEDOT₆, PEDOT₁₂ and PEDOT₁₈, respectively– display monomodal distributions. Samples 4–6 have a “triangular” distribution, referring to the fact that one of the oligomers is predominant and contributes with 9000 repeating units, whereas the other two contribute with 4500 each; we will refer to these distributions as TRI₆, TRI₁₂, and TRI₁₈, respectively. Finally, sample 7 has a uniform distribution, meaning that each oligomer contributes with the same amount of repeating units (6000, except for PEDOT₁₈ which contributes with 5994), which we will refer to as UNI. The rationale behind these oligomer distributions is that they all roughly have the same number of atoms (236000–240000), so that residual size effects (major effects can be safely ruled out on the basis of careful preliminary tests) would affect the results in a similar way. Box sizes are approximately between 15^3 and 16^3 nm³, depending on content and doping state. In doped PEDOT (without PSS) chlorine anions (6000 atoms) are also present in the simulation box to achieve charge neutrality. To model these anions we used the parameters developed by Joung *et al.*^[36]

Additionally, a sample containing both doped PEDOT and PSS has been created (depicted in Figure 2, where the PEDOT

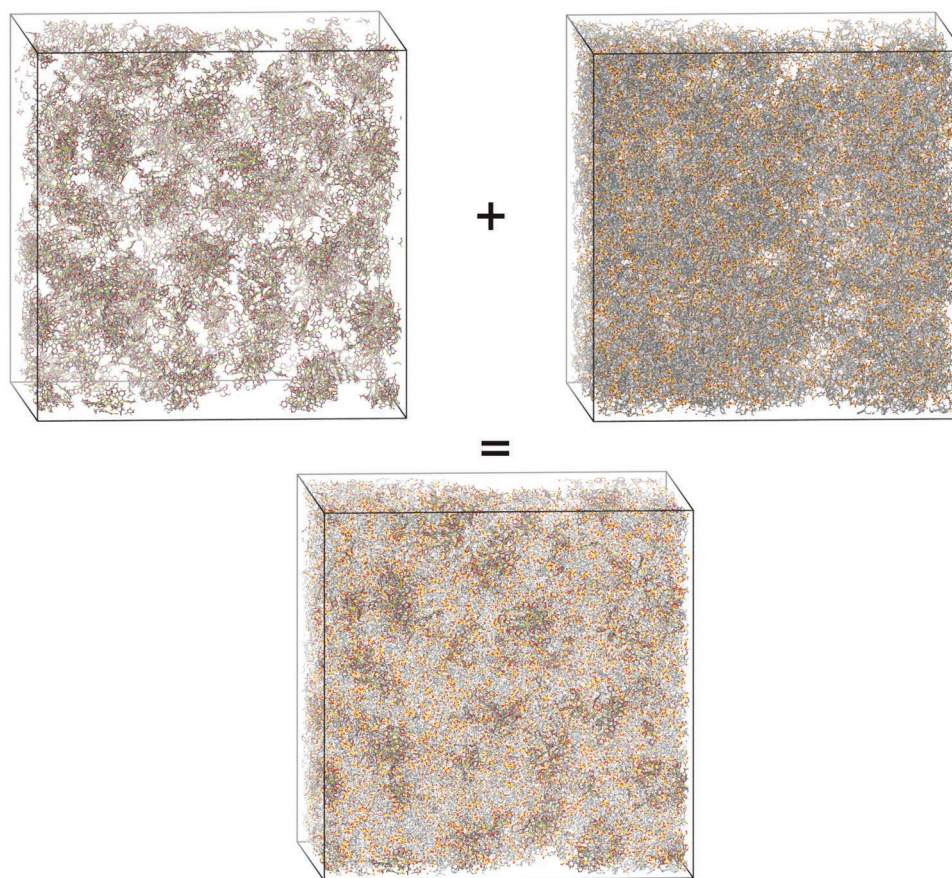


Figure 2. Visual representation of the PEDOT:PSS sample and its two individual phases (PEDOT on the left and PSS on the right). The PSS has been rendered more translucent in the last image to highlight the PEDOT *islands*.

chains follow the previously described UNI distribution, in a mass ratio of 1:2.4. This value is close to the often encountered experimental one (1:2.5) and is also carefully chosen to ensure charge neutrality within the simulation box, without adding any further counterions: as a matter of fact, one PSS chain is composed of 50 repeating units and has a negative net charge $q = -9$ (we will refer to it as PSS_{50}^{-9}). If we insert 180 such molecules and mix them with 4860 PEDOT monomers, the resulting number of atoms is close to 240000 (PSS_{50}^{-9} has 993 atoms). Overall, this sample therefore contains 270 PEDOT_6^{+2} , 135 PEDOT_{12}^{+4} , 90 PEDOT_{18}^{+6} and 180 PSS_{50}^{-9} (where we have now also indicated the charge in PEDOT molecules for additional clarity). In this case, annealing cycles must be appended to the equilibration procedure in order to produce a more realistic morphology. As explained by Makki *et al.*,^[37] the strong electrostatic interactions between positive PEDOT and negative PSS drastically reduce the diffusivity of PEDOT through the sample, making it challenging to find the equilibrium morphology at room temperature. However, one can provide energy to the sample in the form of heat in order to overcome this electrostatic barrier. Therefore, after running the sample in the NPT ensemble for 10 ns (with the same parameters described for the previous cases), we perform several annealing cycles consisting of four steps: using the velocity-rescaling thermostat, we bring the sample to 1100 K, then cool it down to 800 K and subsequently

to 300 K; finally, we run it again in the NPT ensemble at 300 K. This procedure is similar to the one described in the work of Keene *et al.*^[38] and Makki *et al.*,^[37] the differences being the absence of linear ramps to reach the desired temperatures, and that each step is 1 ns long in our case. The rest of the procedure after the equilibration, that is, the AEMD run to compute the thermal conductivity, is similar to the one previously described for pristine PEDOT.

Finally, a sample containing only PSS and sodium cations was also created using the same procedure and parameters described for pristine PEDOT. The same rationale mentioned before applies in this case as well: the sample contains 242 PSS_{50}^{-9} chains and 2178 Na^+ cations,^[39] so that the total number of atoms is in the same range as all the other samples and charge neutrality is achieved.

2.4. Morphological Analysis

The analysis of local crystallinity is carried out in a similar fashion to that described by Cappai *et al.*^[23] The sample crystallinity is quantified by assigning a vector to each EDOT monomer and then calculating the dot product between them. To be more specific, the simulation box is subdivided according to a symmetrical 3D grid and each monomer is assigned an

Table 2. Thermal conductivity of neutral PEDOT samples.

| Sample name | L_{avg} | κ [W m ⁻¹ K ⁻¹] | | | | ρ [g cm ⁻³] |
|---------------------|-----------|---|---------------|---------------|-------------------------------------|------------------------------|
| | | κ_{xx} | κ_{yy} | κ_{zz} | $\kappa_{avg} \pm \text{Std. Dev.}$ | |
| PEDOT ₆ | 6 | 0.097 | 0.092 | 0.093 | 0.094 ± 0.003 | 1.221 |
| TRI ₆ | 8.47 | 0.106 | 0.095 | 0.083 | 0.095 ± 0.012 | 1.075 |
| UNI | 9.82 | 0.111 | 0.116 | 0.118 | 0.115 ± 0.003 | 1.143 |
| TRI ₁₂ | 10.29 | 0.102 | 0.112 | 0.105 | 0.107 ± 0.005 | 1.021 |
| TRI ₁₈ | 11.08 | 0.112 | 0.090 | 0.101 | 0.101 ± 0.011 | 1.080 |
| PEDOT ₁₂ | 12 | 0.124 | 0.127 | 0.122 | 0.125 ± 0.003 | 1.171 |
| PEDOT ₁₈ | 18 | 0.138 | 0.154 | 0.138 | 0.143 ± 0.009 | 1.129 |

orientation vector (labeled \vec{s}_i) connecting two carbon atoms at the two ends of the thiophene ring; the dot product is calculated inside a fixed radius $r_0 = 5 \text{ \AA}$ around each vector, according to the formula

$$C(\vec{r}) = \frac{1}{N} \sum_{|\vec{r}-\vec{r}_j| < r_0} |\vec{s}_i(\vec{r}) \cdot \vec{s}_j(\vec{r}_j)| \quad (6)$$

where \vec{r} is the position of a carbon and N is the total number of EDOT monomers in the sample. According to Equation 6, a high value of $C(\vec{r})$ means that there is local alignment, while a low one means that there is almost none. We perform this calculation within a reasonably large sub-region of the same size for all the samples, in order to be able to make meaningful comparisons.

Radial distribution functions (RDF) are computed between sulfur atoms belonging to different oligomers and between chlorine anions, respectively, while X-Ray Diffraction (XRD) spectra are obtained by using the Debyer code.^[40]

3. Results and Discussion

3.1. Neutral PEDOT

Neutral PEDOT has a limited practical interest, because in TE applications samples are doped in order to guarantee a sizeable electrical conductivity. Doping in organic semiconductors is typically concomitant with the polymerization process and implies the presence of counterions, of which there are many examples and which can produce different outcomes in the overall morphology^[41] (and thus, both in the electrical and thermal properties), depending on their nature, for example, molecular or polymeric. In other words, at variance with inorganic semiconductors where doping is obtained by adding impurities to the nominally intrinsic (i.e., neutral) sample, in PEDOT polymerization and doping occur simultaneously and a set of closely interconnected parameters governs the final properties of the material. Therefore, studying the morphology and thermal conductivity of neutral PEDOT is very useful in that it serves as a means of comparison, allowing us to later separately address the effect of charge doping and of a specific polymeric counterion (PSS), and to analyze the possible correlations between morphological and thermal features.

The calculated values of the thermal conductivity, κ , of PEDOT in its neutral charge state are summarized in **Table 2**. As can be seen in **Figure 3**, our results highlight a direct dependence of κ with L_{avg} (measured in monomer units), particularly for what the monomodal distributions are concerned (i.e., $L_{avg} = 6, 12, \text{ and } 18$). Therefore, the most conductive system is PEDOT₁₈, consisting exclusively of the longest chains considered in this work. Accordingly, the lower conductivity among monomodal samples is found for PEDOT₆. Multimodal distributions, on the other hand, roughly exhibit a weighted average κ , though it is more difficult to highlight a clear trend. Indeed, we found that κ_{UNI} is larger than the values obtained for TRI₁₂ and TRI₁₈, despite it has average shorter PEDOT chains (see Table 1). The overall correlation between thermal conductivity and chain length that we found agrees well with the previous report of Cappai *et al.*,^[22] though the values that we obtained

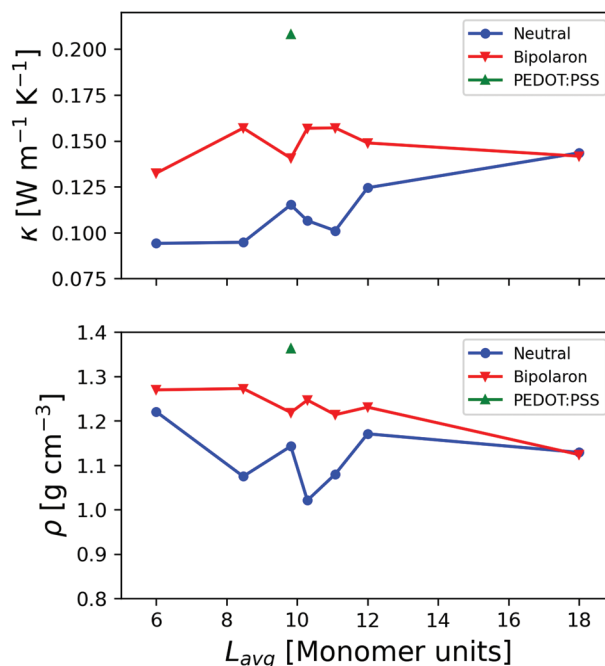


Figure 3. Thermal conductivity, κ , and density, ρ , of both neutral, doped PEDOT and PEDOT:PSS as a function of the average chain length L_{avg} of the samples.

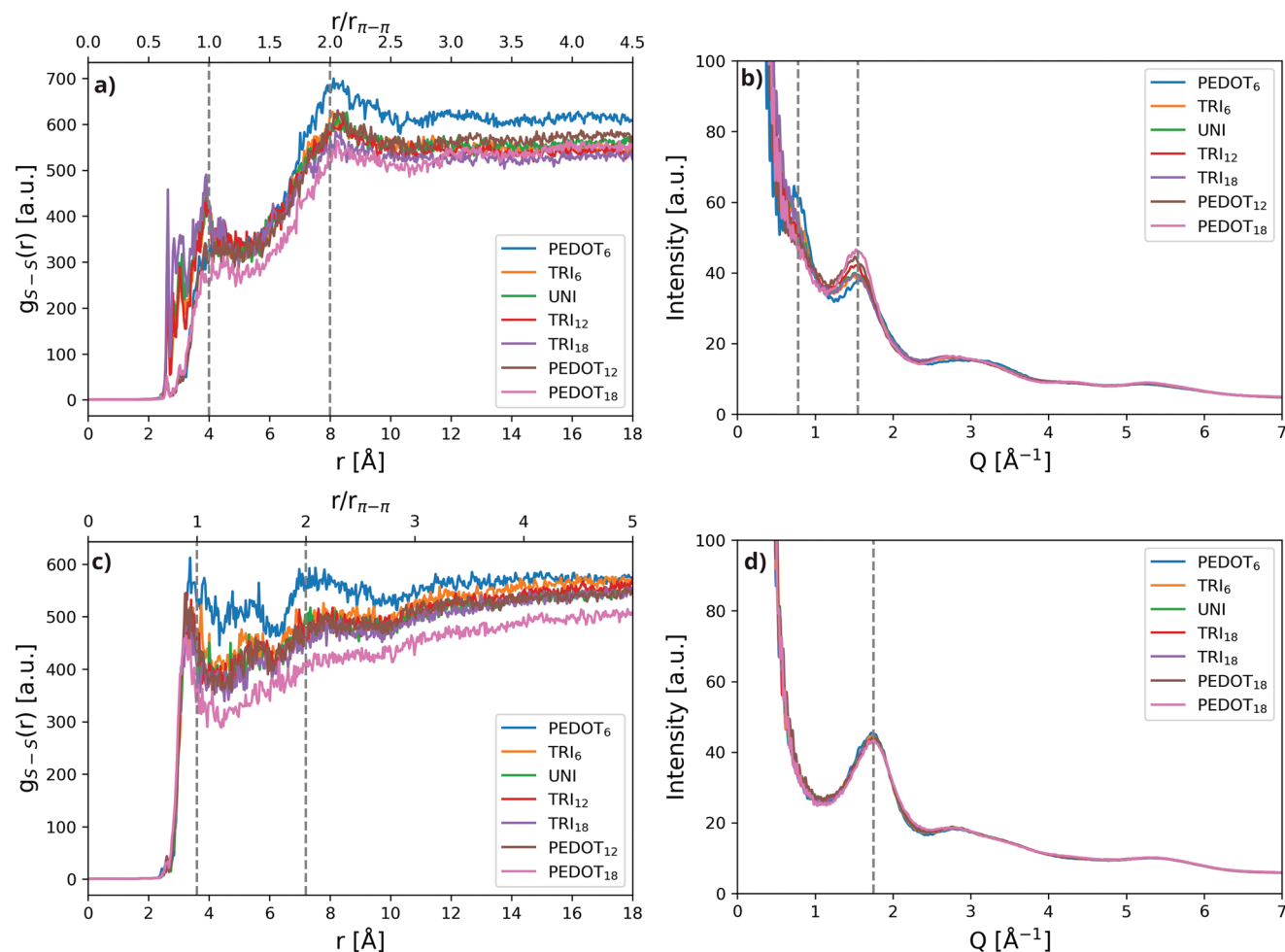


Figure 4. Radial distribution functions $g_{S-S}(r)$ calculated between sulphur atoms belonging to different oligomers and X-ray diffraction spectra for neutral (panels a,b) and doped samples (panels c,d).

with the newly developed force field differ considerably. Note that there is no positive correlation between κ and ρ , as one could expect. As a matter of fact, the least conductive sample, PEDOT₆, exhibits the largest density.

In some samples we observe a certain degree of thermal conductivity anisotropy between the independently computed values of κ_{xx} , κ_{yy} and κ_{zz} . Such an anisotropy, previously observed in PEDOT,^[23] has been attributed to a local chain alignment toward preferential directions resulting in a corresponding favorite direction for heat conduction. This phenomenon, mainly observed for relatively long PEDOT chains, is expected to be partially due to the limited size of the simulation cells. We expect that by increasing the cell dimension, such a local anisotropy would be canceled-out resulting in an overall isotropic thermal conductivity, as expected in an amorphous material.

In **Figure 4**, we display the RDF calculated between sulfur atoms that belong to different oligomers. It shows two distinct peaks at 4 and 8 Å for all samples, albeit of different intensity. The position of the peaks suggests that the π -stacking distance between neutral PEDOT chains is ≈ 4 Å; the number of peaks implies that the π - π domains consist of up to 3 chains.

These conclusions are corroborated by the XRD data, where the π -stacking distance can be obtained as $d_{\pi-\pi} = 2\pi/Q$, with Q being the momentum transfer associated with the impact of the X-rays. As can be seen in **Figure 4**, we found a peak for $Q \approx 1.55 \text{ \AA}^{-1}$, which gives $d_{\pi-\pi} \approx 4 \text{ \AA}$, while the peak for $Q \approx 0.8 \text{ \AA}^{-1}$, only distinguishable for PEDOT₆, gives a distance of 8 Å, which is approximately equal to $2d_{\pi-\pi}$.

3.2. Doped PEDOT

We now move to the study of doped PEDOT, considering specifically its bipolaronic charge state. Although it has been found that polarons and bipolarons can coexist in doped PEDOT,^[42] a reliable model to account for these two charge states simultaneously is not available yet. In any case, we believe that this model still holds significance with respect to what we set out to investigate.

In this subset of doped systems the net charge of PEDOT is balanced by Cl⁻ counterions. We do not expect the specific distribution of Cl⁻ ions (and thus the parameterization employed) to have a significant effect on the thermal

Table 3. Thermal conductivity of doped PEDOT and PEDOT:PSS samples.

| Sample name | Thermal Conductivity [W m ⁻¹ K ⁻¹] | | | | ρ [g cm ⁻³] |
|---------------------|---|------------|------------|-------------------------------------|------------------------------|
| | κ_x | κ_y | κ_z | $\kappa_{avg} \pm \text{Std. Dev.}$ | |
| PEDOT ₆ | 0.139 | 0.135 | 0.123 | 0.132 ± 0.008 | 1.270 |
| TRI ₆ | 0.152 | 0.156 | 0.163 | 0.157 ± 0.006 | 1.273 |
| UNI | 0.141 | 0.133 | 0.149 | 0.141 ± 0.008 | 1.219 |
| UNI:PSS | 0.209 | 0.206 | 0.210 | 0.208 ± 0.002 | 1.363 |
| TRI ₁₂ | 0.156 | 0.148 | 0.167 | 0.157 ± 0.009 | 1.247 |
| TRI ₁₈ | 0.145 | 0.168 | 0.159 | 0.157 ± 0.012 | 1.214 |
| PEDOT ₁₂ | 0.137 | 0.158 | 0.152 | 0.149 ± 0.011 | 1.231 |
| PEDOT ₁₈ | 0.140 | 0.143 | 0.142 | 0.142 ± 0.002 | 1.124 |

conductivity of PEDOT, with respect to similar anions. A more massive polyanion such as PSS, on the other hand, is expected to have a stronger impact; this case is discussed in detail in the next section.

The values we obtained, shown in Figure 3 and summarized in **Table 3**, describe a more complex situation with respect to the neutral case and no straightforward correlation with the average chain length emerges. Indeed, here we observe a competition between two effects, namely the average chain length and the density. A higher density implies that the polymer chains are on average closer to each other, which is expected to facilitate thermal transport.^[43] At the same time, as we saw in our study of neutral PEDOT, longer average chain length promote larger κ . However, as can also be seen in Figure 3 (lower panel), our calculations also show that the density of our samples tends to decrease when increasing L_{avg} and thus longer chains produce less dense samples, effectively mitigating the increase in κ . This happened to some extent in the neutral sample as well, but this effect appears to be amplified in this case. As noted by Micheals *et al.*, both neutral and doped PEDOT oligomers adopt an extended conformation in the absence of external disturbances (i.e., isolated). However, steric effects in PEDOT films (with or without PSS, neutral or doped) are sufficient to disrupt the rodlike conformation (especially in neutral oligomers, due to their lower torsional barriers and local minima ($\phi = \{45^\circ, 315^\circ\}$)).^[26] These effects appear to become more and more significant as the content of longer oligomers increases, making it difficult to occupy the space efficiently (i.e., resulting in lower densities). In the charged state, however, PEDOT adopts the quinoid structure and is comparatively stiffer, due to the larger barriers for rotations around inter-monomer bond. Hence, the somewhat stronger negative correlation between density and chain length highlighted by the data of Figure 3.

Therefore, PEDOT₆, which has the lowest L_{avg} , shows the second highest ρ and a the lowest κ . Similarly, PEDOT₁₈ has the highest L_{avg} and the lowest ρ , which result in the second lowest κ . The PEDOT₁₂ sample, on the other hand, combines intermediate L_{avg} and rather high ρ and is thus the more conductive monomodal distribution. The highest κ is obtained with the TRI_l samples ($l = 6, 12, 18$), which have a less than intermediate L_{avg} and rather high ρ . It should also be highlighted that there is a general increase of κ upon doping, regardless of L_{avg} (i.e., $\kappa_{doped} \geq \kappa_{neutral} \forall L_{avg}$). Also in this case, κ_{UNI} deviates

from the overall trend and is lower than the one of samples with similar average chain length and density.

The radial distribution function depicted in 4 shows two peaks for all samples except PEDOT₁₈, which only has one, and they are at ≈ 3.6 and ≈ 7.2 Å respectively. Additionally, if we take a look at the calculated XRD patterns in Figure 4, we can see a halo centered at $Q \approx 1.75$ Å⁻¹ which corresponds to $d_{\pi-\pi} \approx 3.6$ Å. This is in almost perfect agreement with the XRD experiments on PEDOT in the literature.^[44,45] It is worth noting that, in contrast to the undoped scenario, all these doped PEDOT XRD patterns coincide almost perfectly. This may have implications for the improvement mechanism of the electrical conductivity: not only does doping introduce additional charge carriers, but it also reduces the π - π distance, which means that the hopping probability will be greatly enhanced. We suggest that the difference in π - π distance depending on the doping state might arise from the fact that the (even partially) π -stacked regions might be subject to some degree of “quenched” by the surrounding counterions and as a result doped chains tend to be closer to each other. We calculated additional radial distribution functions between chlorine anions in some of our doped samples (depicted in **Figure 5**). Three main peaks can be spotted, with varying breadth: the first one is quite broad and is centered around 7.2 Å, the second is the narrowest and is centered at 10 Å, while the third is almost invisible and is located around 14–14.5 Å. While the interpretation is not straightforward, the fact that the same peaks appear in different samples tells us that this is a specific signature of such doped amorphous systems. We propose, tentatively, to relate the first and last peak to the PEDOT π - π distance, while the central peak could be related to the lamellar length. Further investigations, beyond the scope of this work, are needed to be more conclusive.

We also present the results for the local crystallinity calculations, as described in the previous section. The color maps shown in **Figure 6** give us a qualitative picture of the morphology of PEDOT as a function of doping level and average chain length (each short black segment represents one monomer). By analyzing these maps, we can qualitatively observe for neutral PEDOT a slight crystallinity decrease as a function of the average chain length (i.e., there are less high crystallinity regions, depicted in light blue, as the chain length increases); on the other hand, in doped PEDOT the overall crystallinity seems essentially unaffected by the average chain length. These

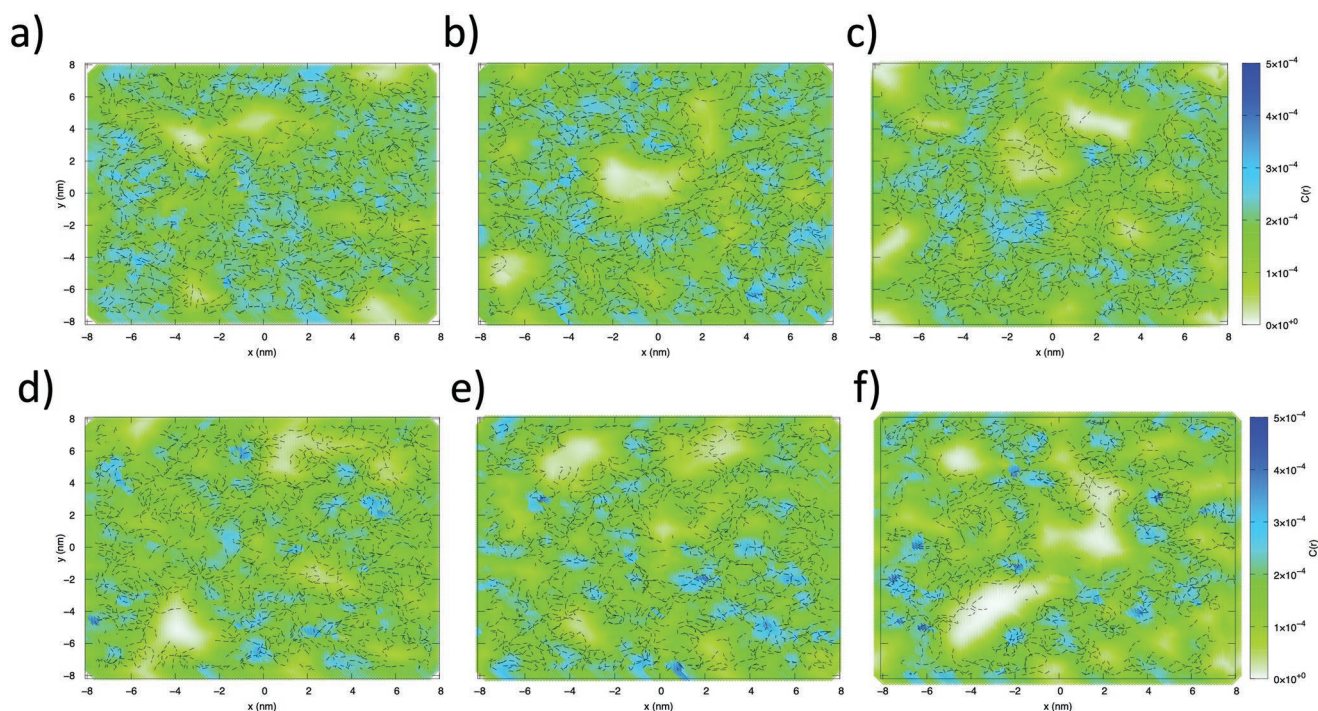


Figure 5. Local crystallinity maps computed on slabs having a thickness of 0.5 nm for neutral PEDOT₆, PEDOT₁₂, and PEDOT₁₈ a–c) and for doped PEDOT₆, PEDOT₁₂, and PEDOT₁₈ d–f).

somewhat qualitative observations are further corroborated by a more quantitative analysis where for each sample we estimated the volume of the simulation cell for which $C(r)$ is larger than a given threshold value [equal to 0.002 corresponding to about half of the span of values taken by $C(r)$]. This analysis confirms that for neutral PEDOT the crystallinity fraction slightly decreases from $\approx 40\%$ for PEDOT₆ down to $\approx 31\%$ for PEDOT₁₂ and finally to $\approx 24\%$ for PEDOT₁₈. The same analysis performed for doped PEDOT shows very small crystallinity variations depending on the average chain length, that is, $\approx 20\%$ for PEDOT₆, $\approx 19\%$ for PEDOT₁₂ and $\approx 17\%$ for PEDOT₁₈. We therefore conclude that for both neutral and doped PEDOT, the overall micromorphology and corresponding crystallinity seem to be slightly affected by the average chain lengths.

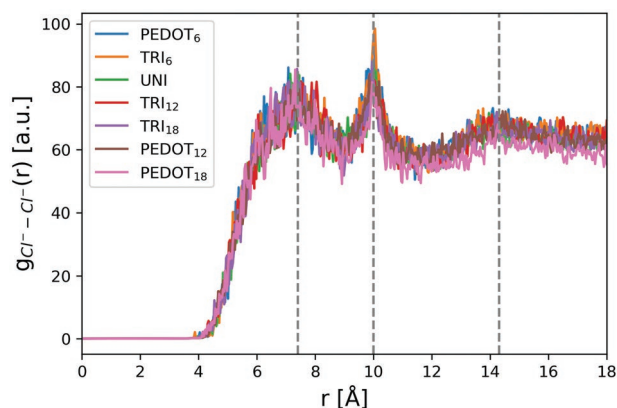


Figure 6. RDF of chlorine anions in doped samples.

3.2.1. PEDOT:PSS

As can be noted in both Figure 3 and Table 3, the addition of PSS instead of chlorine anions visibly enhances the thermal conductivity of the doped sample labeled UNI. As a matter of fact, it is the highest obtained throughout this work. We trace back this change to an increase in the density and to the intrinsically higher thermal conductivity of PSS itself with respect to PEDOT: as a matter of fact, we obtained a value of $0.25 \pm 0.02 \text{ W m}^{-1} \text{ K}^{-1}$ for PSS. The latter is a very important point, neglected so far, because it implies that also the lattice component of the thermal conductivity, and not only the electronic one, increases due the presence of PSS.

Just like in the previous cases, we computed the radial distribution function between sulfur atoms belonging to different PEDOT oligomers, XRD spectrum and local crystallinity map. The RDF in Figure 7a shows a first clear peak between 3.3 and 3.6 Å and a second one centered around 7.2 Å, though with severely reduced intensity. The XRD spectra are calculated individually for PEDOT, PSS, and PEDOT:PSS, shown in 7b. The PEDOT spectrum shows a wide and extremely weak halo approximately between 1.5 and 1.8 Å⁻¹, which is compatible with the RDF peaks and corresponds to the π - π characteristic length of PEDOT. This is in contrast with what happened in the presence of chlorine anions, which produced a more definite peak: this can be attributed to the fact that our PSS molecules possess sulfonate and sulfonic acid groups (i.e., charged and uncharged, respectively) along their chains, which give rise to different interactions with different parts of PEDOT molecules (as shown by Yildirim *et al.*^[20]). The PSS spectrum, conversely, shows one (less) broad and (more) intense peak

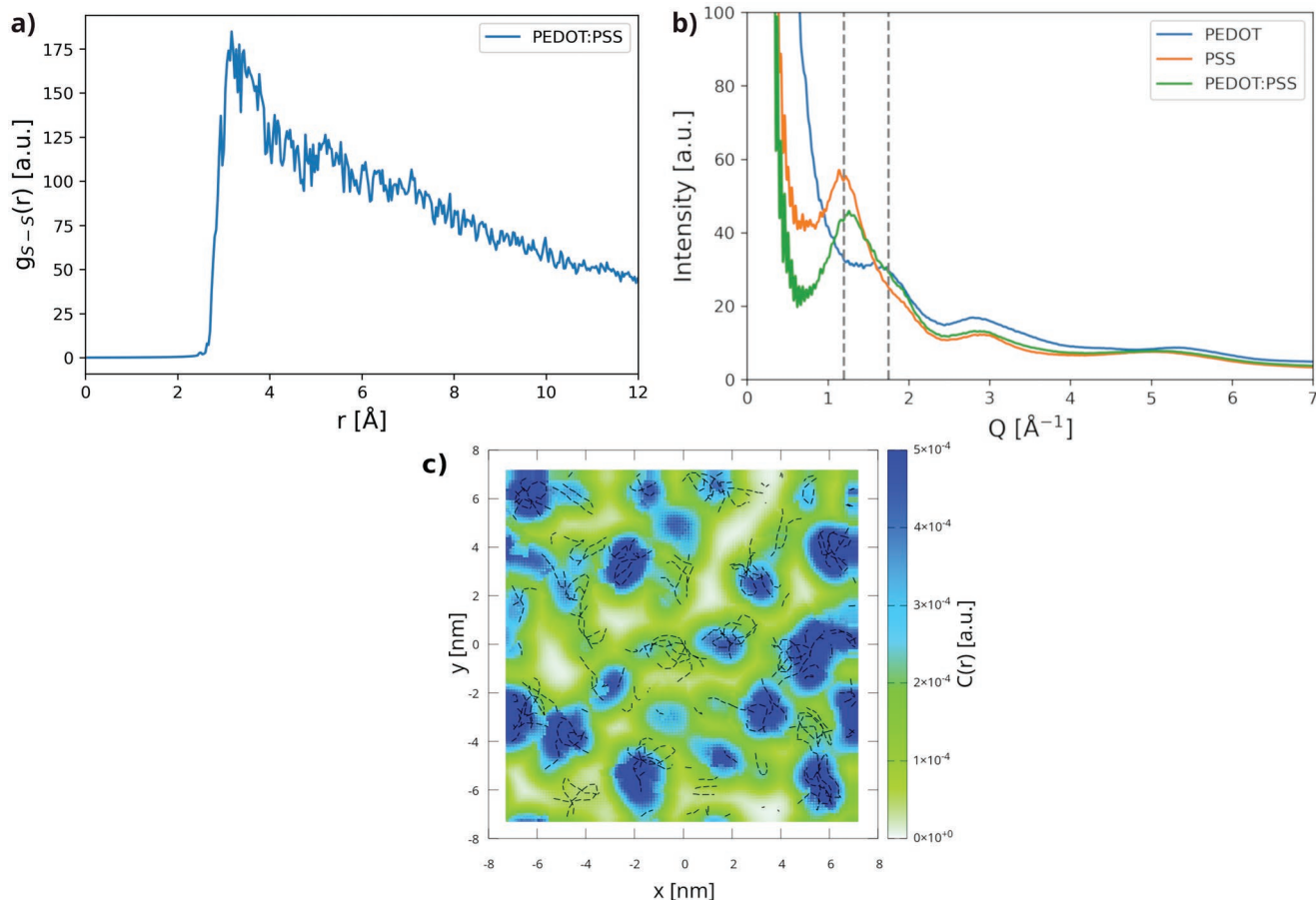


Figure 7. Images a–c) refer to the only PEDOT:PSS sample. a) RDF calculated between sulphur atoms belonging to different PEDOT oligomers. b) X-ray diffraction spectra of PEDOT, PSS and PEDOT:PSS combined. c) Local crystallinity map.

around 1.2 \AA^{-1} , which corresponds to a characteristic length of 5.2 \AA : we associate this with the π - π stacking distance between the benzene rings of PSS. This is almost coincident with experimental values.^[44,45] The weak PEDOT halo is almost completely hidden in the overall spectrum. The local crystallinity map in 7c shows several blue spots having a size of $\sim 2 \text{ nm}$, in which some small PEDOT aggregates (≈ 6 chains per aggregate) are located (this justifies the RDF approaching low values around 10 \AA , since for greater radii there is hardly any PEDOT). These areas have a significantly higher degree of local order than the pristine PEDOT samples, although it should be clear by looking at the black dashed lines representing the PEDOT backbones, that they are not perfectly crystalline. This is in agreement with what Makki and Troisi^[37] found, using the same force field parameters of the present work. They put a massive effort into validating the relaxation procedure already developed in the work by Keene *et al.*,^[38] producing realistic PEDOT:PSS morphologies based on Atomic Force Microscopy and XRD experimental data. Their morphologies also feature such aggregates, although our PEDOT “islands” do not appear to be entirely interconnected through a π - π network. Nevertheless, due to the fact that we have employed the same procedure for each sample (except PEDOT:PSS for which we applied cycles of annealing), all the values are directly comparable with each other, meaning that we

are able to assess what we set out to in the first place (i.e., the impact of doping on lattice thermal conductivity of PEDOT:PSS).

For these samples we only considered a uniform distribution of PEDOT chain lengths, mostly because of the great numerical complexity deriving from the generation of samples with such long PSS chains. Yet, to a first approximation, we expect the trends unveiled in Section 3.2 to hold here too.

4. Conclusion

We set out to create amorphous PEDOT samples in its neutral and doped state, both in the presence of small chlorine anions and of the large polyanion PSS, varying the length of the constituent PEDOT chains. We calculated their lattice thermal conductivity and analyzed some of their morphological properties in order to find possible correlations between them. We have found charge doping to be responsible for overall higher thermal conductivity, for the reduction in the characteristic π - π distance, from 4 to 3.6 \AA (with the implications that this has on hopping probability and, therefore, electrical conductivity) and for evident discrepancies in the spatial distribution of PEDOT, especially when it comes to samples with short chains. However, the different behavior

of κ in neutral and doped PEDOT can be ultimately linked to their different relationship between average chain length and density. In neutral PEDOT we observe a weak negative correlation between average chain length and density, which is not strong enough to revert the positive correlation existing between average chain length and lattice thermal conductivity. On the contrary, in doped PEDOT the negative correlation between average chain length and density is stronger and gives rise to a maximum for the thermal conductivity at less than intermediate average chain lengths. This different behavior can, in turn, be traced back to the change in stiffness when considering neutral and doped PEDOT. As previously reported,^[26] neutral PEDOT is more flexible, due to the lower torsional barrier of the backbone, which derives from the aromatic conjugation structure. Conversely, in its bipolaronic charge state, PEDOT adopts the quinoid structure and the rotational freedom around inter-monomer bonds is reduced. Nonetheless, steric effects in films (regardless of the presence of PSS) are enough to overcome the torsional barriers and they become predominant when increasing the content of longer oligomers, producing films with both lower density and thermal conductivity. Note that this conformational transition cannot be captured by using GAFF bonded parameters and only changing the atomic partial charges. For this reason, only an ad hoc reparameterization such as the one used in the present work is able to reproduce this kind of behavior. The addition of PSS to the mixture (with a PEDOT:PSS mass ratio of 1:2.4) gives rise to morphologies with small aggregates of PEDOT (≈ 6 chains) with increased (though not perfect) local order, embedded in a matrix of PSS. We suggest that the thermal conductivity is increased due to the intrinsically better transport properties of PSS with respect to PEDOT.

We expect that these results to be useful to better understand the distinct contributions of charge doping and of PSS itself on the lattice thermal conductivity of PEDOT:PSS complexes, thus helping the design of efficient TE materials based on these polymers.

Supporting Information

Supporting Information is available from the Wiley Online Library or from the author.

Acknowledgements

This work was financially supported by the European Commission through the Marie Skłodowska–Curie projects HORATES (GA-955837), by MCIN/AEI/10.13039/501100011033 under grant PID2020-119777GB-I00, and the Severo Ochoa Centres of Excellence Program under grant CEX2019-000917-S, and by the Generalitat de Catalunya under grant no. and 2017 SGR 1506. We thank the Centro de Supercomputación de Galicia (CESGA) for the use of their computational resources. The authors would like to thank Wesley Micheals and Jian Qin for the insights provided about the force field employed in this work, Mariano Campoy-Quiles, Simone Fabiano, Christian Müller, Igor Zozoulenko for useful discussions. The author P.S.F. would like to extend his personal thanks to Marc Domingo Cabases for his advice on some of the technicalities involved in this research.

Conflict of Interest

The authors declare no conflict of interest.

Data Availability Statement

The data that support the findings of this study are available from the corresponding author upon reasonable request.

Keywords

molecular dynamics, PEDOT:PSS, thermal conductivity, thermoelectrics

Received: December 28, 2022

Revised: February 17, 2023

Published online: March 27, 2023

- [1] C. K. Chiang, C. R. Fincher, Y. W. Park, A. J. Heeger, H. Shirakawa, E. J. Louis, S. C. Gau, A. G. MacDiarmid, *Phys. Rev. Lett.* **1977**, 39, 1098.
- [2] M. E. Roberts, S. C. B. Mannsfeld, R. M. Stoltenberg, Z. Bao, *Org. Electron.* **2009**, 10, 377.
- [3] M. P. de Jong, L. J. van IJzendoorn, M. J. A. de Voigt, *Appl. Phys. Lett.* **2000**, 77, 2255.
- [4] S. Na, S. Kim, J. Jo, D. Kim, *Adv. Mater.* **2008**, 20, 4061.
- [5] L. Zhang, K. Yang, R. Chen, Y. Zhou, S. Chen, Y. Zheng, M. Li, C. Xu, X. Tang, Z. Zang, K. Sun, *Adv. Electron. Mater.* **2020**, 6, 1900648.
- [6] H. Tang, P. Lin, H. L. W. Chan, F. Yan, *Biosens. Bioelectron.* **2011**, 26, 4559.
- [7] F. Wu, P. Li, K. Sun, Y. Zhou, W. Chen, J. Fu, M. Li, S. Lu, D. Wei, X. Tang, Z. Zang, L. Sun, X. Liu, J. Ouyang, *Adv. Electron. Mater.* **2017**, 3, 1700047.
- [8] X. Fan, W. Nie, H. Tsai, N. Wang, H. Huang, Y. Cheng, R. Wen, L. Ma, F. Yan, Y. Xia, *Adv. Sci.* **2019**, 6, 1900813.
- [9] Y. Yang, H. Deng, Q. Fu, *Mater. Chem. Front.* **2020**, 4, 3130.
- [10] M. N. Gueye, A. Carella, J. Faure-Vincent, R. Demadrille, J.-P. Simonato, *Prog. Mater. Sci.* **2020**, 108, 100616.
- [11] D. Kim, Y. Kim, K. Choi, J. C. Grunlan, C. Yu, *ACS Nano* **2010**, 4, 513.
- [12] C. Wang, K. Sun, J. Fu, R. Chen, M. Li, Z. Zang, X. Liu, B. Li, H. Gong, J. Ouyang, *Adv. Sustainable Syst.* **2018**, 2, 1800085.
- [13] Y. Shu, G. O. Odunmbaku, Y. He, Y. Zhou, H. Cheng, J. Ouyang, K. Sun, *Appl. Phys. Lett.* **2021**, 118, 103902.
- [14] J. Ouyang, Q. Xu, C.-W. Chu, Y. Yang, G. Li, J. Shinar, *Polymer* **2004**, 45, 8443.
- [15] Z. Fan, J. Ouyang, *Adv. Electron. Mater.* **2019**, 5, 1800769.
- [16] O. Bubnova, Z. U. Khan, A. Malti, S. Braun, M. Fahlman, M. Berggren, X. Crispin, *Nat. Mater.* **2011**, 10, 429.
- [17] G. H. Kim, L. Shao, K. Zhang, K. P. Pipe, *Nat. Mater.* **2013**, 12, 719.
- [18] Z. Fan, D. Du, X. Guan, J. Ouyang, *Nano Energy* **2018**, 51, 481.
- [19] W. Michaels, Y. Zhao, J. Qin, *Macromolecules* **2021**, 54, 3634.
- [20] E. Yildirim, G. Wu, X. Yong, T. L. Tan, Q. Zhu, J. Xu, J. Ouyang, J.-S. Wang, S.-W. Yang, *J. Mater. Chem. C* **2018**, 6, 5122.
- [21] W. Shi, T. Zhao, J. Xi, D. Wang, Z. Shuai, *J. Am. Chem. Soc.* **2015**, 137, 12929.
- [22] A. Cappai, A. Antidormi, A. Bosin, D. Narducci, L. Colombo, C. Melis, *Phys. Rev. Materials* **2020**, 4, 035401.
- [23] A. Cappai, A. Antidormi, A. Bosin, D. Galliani, D. Narducci, C. Melis, *Phys. Chem. Chem. Phys.* **2021**, 21, 8580.
- [24] A. Crnjar, C. Melis, L. Colombo, *Phys. Rev. Mater.* **2018**, 2, 015603.
- [25] C. Genovese, A. Antidormi, R. Dettori, C. Caddeo, A. Mattoni, L. Colombo, C. Melis, *J. Phys. D: Appl. Phys.* **2017**, 50, 494002.

- [26] W. Michaels, Y. Zhao, J. Qin, *Macromolecules* **2021**, *54*, 5354.
- [27] M. Modarresi, J. F. Franco-Gonzalez, I. Zozoulenko, *Phys. Chem. Chem. Phys.* **2019**, *21*, 6699.
- [28] M. Modarresi, J. F. Franco-Gonzalez, I. Zozoulenko, *Phys. Chem. Chem. Phys.* **2018**, *20*, 17188.
- [29] W. Humphrey, A. Dalke, K. Schulten, *J. Mol. Graphics* **1996**, *14*, 33.
- [30] J. Stone, Master's thesis, University of Missouri-Rolla, **1998**.
- [31] J. Wang, R. Wolf, J. Caldwell, P. Kollman, D. Case, *J. Comput. Chem.* **2004**, *25*, 1157.
- [32] E. Lampin, P. L. Palla, P.-A. Francioso, F. Cleri, *J. Appl. Phys.* **2013**, *114*, 033525.
- [33] C. Melis, R. Dettori, S. Vandermeulen, L. Colombo, *Eur. Phys. J. B* **2014**, *87*, 96.
- [34] R. Agbaoye, P. Adebambo, J. Akinlami, T. Afolabi, S. Z. Karazhanov, D. Ceresoli, G. Adebayo, *Comput. Mater. Sci.* **2017**, *139*, 234.
- [35] A. P. Thompson, H. M. Aktulga, R. Berger, D. S. Bolintineanu, W. M. Brown, P. S. Crozier, P. J. in 't Veld, A. Kohlmeyer, S. G. Moore, T. D. Nguyen, R. Shan, M. J. Stevens, J. Tranchida, C. Trott, S. J. Plimpton, *Comp. Phys. Comm.* **2022**, *271*, 108171.
- [36] I. S. Joung, T. E. Cheatham, *J. Phys. Chem. B* **2008**, *112*, 9020.
- [37] H. Makki, A. Troisi, *J. Mater. Chem. C* **2022**, *10*, 16126.
- [38] S. T. Keene, W. Michaels, A. Melianas, T. J. Quill, E. J. Fuller, A. Giovannitti, I. McCulloch, A. A. Talin, C. J. Tassone, J. Qin, A. Troisi, A. Salleo, *J. Am. Chem. Soc.* **2022**, *144*, 10368.
- [39] M. J. L. Sangster, R. M. Atwood, *J. Phys. C: Solid State Phys.* **1978**, *11*, 1541.
- [40] <https://github.com/wojdyr/debyer>.
- [41] G. Zotti, S. Zecchin, G. Schiavon, F. Louwet, L. Groenendaal, X. Crispin, W. Osikowicz, W. Salaneck, M. Fahlman, *Macromolecules* **2003**, *36*, 3337.
- [42] B. D. Paulsen, R. Wu, C. J. Takacs, H.-G. Steinrück, J. Strzalka, Q. Zhang, M. F. Toney, J. Rivnay, *Adv. Mater.* **2020**, *32*, 2003404.
- [43] D. Hands, K. Lane, R. P. Sheldon, *J. Polym. Sci., Polym. Symp.* **1973**, *42*, 717.
- [44] N. Kim, B. H. Lee, D. Choi, G. Kim, H. Kim, J. Kim, J. Lee, Y. H. Kahng, K. Lee, *Phys. Rev. Lett.* **2012**, *109*, 106405.
- [45] E. Hosseini, V. Ozhukil Kollath, K. Karan, *J. Mater. Chem. C* **2020**, *8*, 3982.